Mon. Not. R. Astron. Soc. **000**, 1–11 (2006) Printed 7 February 2006 (MN LaTeX style file v2.2)

High resolution X-ray spectroscopy of bright O type stars

L. M. Oskinova,⋆ A. Feldmeier, W.-R. Hamann
Astrophysik, Universität Potsdam, Am Neuen Palais 10, Potsdam 14469, Germany

Accepted . Received ; in original changedorm

ABSTRACT

In this paper we reproduce the shape of X-ray emission lines observed in single non-magnetic O stars using a clumped wind model. The Chandra HETGS/MEG spectra of ζ Pup, ξ Per, ζ Ori, and ζ Oph are analyzed. From the line ratios of He-like ions the X-ray line formation regions are constrained to be located in the acceleration part of the stellar winds. To calculate the wind opacity at X-ray wavelengths for each star we use the NLTE stellar atmosphere model PoWR. The stellar parameters and wind opacities are then used as input parameters for our 2-D numerical model of a stochastic, inhomogeneous wind consisting of radially compressed shell fragments. The model line profiles are symmetric, blueshifted, and similar across the spectrum, exactly as observed in the spectra of our sample stars. We conclude that X-ray emission line profiles observed in O stars can be explained by the radiative transfer in clumped stellar winds.

Key words: X-rays:stars, stars:individual:ζ Pup, ζ Ori, ξ Per, ζ Oph

1 INTRODUCTION

Young and massive O-type stars possess strong stellar winds. The winds are fast, with typical velocities up to 2500 km/s, and dense, with mass-loss rates $\dot{M} \sim 10^{-7} M_{\odot}/\mathrm{yr}$. The driving mechanism for the mass-loss from OB stars has been identified with radiation pressure on spectral lines (Castor et al. 1975). However, it was pointed out early (Lucy & Solomon 1970) and later further investigated (Owocki & Rybicki 1984) that the stationary solution for a line-driven wind is unstable; small perturbation grow quickly and result in strong shocks giving rise to the production of hot gas and emitting of X-rays.

X-rays from hot OB type stars were discovered by the Einstein X-ray observatory (Harnden et al. 1979; Seward et al. 1979). A large number of OB type stars was detected by the Rosat All Sky Survey (Berghöfer et al. 1996), providing firm evidence that the X-ray emission is intrinsic for strong stellar winds. The low resolution Rosat spectrum of the O-type supergiant ζ Pup was modeled by Hillier et al. (1993). In order to explain the apparent weakness of absorption in the spectrum, Hillier et al. (1993) postulated that the X-rays are emitted far out in the stellar wind, at distances larger that 100 R_*, by an optically thin shell expanding at constant velocity. The emission from such shell would produce a broad box-like line.

A broad rectangular line profile is distinctly different from a line arising in the wind acceleration zone and attenuated in the wind. MacFarlane et al. (1991) have shown that an emission line attenuated in a spherically symmetric and smooth stellar wind has a characteristic blueshifted and skewed profile. Ignace (2001) demonstrated that the line asymmetry correlates with the wind opacity and density. Since atomic opacity is wavelength dependent, the lines are expected to differ in shape across the spectrum, with larger blueshift for the lines with higher opacity.

X-ray generation in the wind acceleration zone is predicted in the model by Feldmeier et al. (1997), who showed from hydrodynamic simulations that dense cool shells of gas form in deep wind regions. Collisions of these shells can lead to strong shocks. X-rays originate from radiatively cooling zones behind the shock fronts. The hot X-ray emitting plasma is thermal, has a small filling factor, and is optically thin. The produced X-rays can be significantly attenuated by the overlying cool stellar wind. Hence the blueshifted lines are expected.

High-resolution X-ray spectra of O-type stars were obtained for the first time by the Chandra X-ray observatory (Waldron & Cassinelli 2001). The resolved emission line profiles offer a stringent test for the theory. The analysis of the line ratios from He-like ions in ζ Ori and ζ Pup constrained the regions of X-ray formation relatively close to the stellar surface. The broadening of the lines was measured to be less than corresponding to the maximum velocity, confirming their origin in the wind acceleration zone. Line blueshifts were also detected, indicating wind attenuation (Cassinelli et al. 2001).

However, the data revealed that the line blueshifts do not change significantly for lines at different wavelengths in contrast to what was expected (Waldron & Cassinelli 2001; Cassinelli et al. 2001). Moreover, line fits using the conventional homogeneous wind model demonstrated that in order to reproduce the lines observed in non-magnetic single O stars, a significant reduction of empirically determined mass-loss rates is required (Kramer et al. 2003).

In clumped winds the empirical mass-loss estimates shall be generally reduced by factors of a few (Hamann & Koesterke 1998). Lower mass-loss rates from O stars were suggested by several au-

⋆ E-mail: lida@astro.physik.uni-potsdam.de

© 2006 RAS

thors on the basis of growing observational and theoretical evidence that O star winds are strongly clumped (Repolust et al. 2004; Bouret et al. 2005; Fullerton et al. 2005).

Clumping of the wind seriously affects the radiative transfer (Pomraning 1991). The transport of X-rays in clumpy media was studied analytically and numerically by Feldmeier et al. (2003) and Oskinova et al. (2004). In the present paper we apply this line transfer formalism to model the X-ray emission line profiles observed in the spectra of the prominent single O stars ζ Pup, ξ Per, ζ Ori, and ζ Oph. The NLTE stellar atmospheres code PoWR (Hamann & Gräfener 2004) is employed to calculate the cool wind opacity for each star. Using this opacity and corresponding stellar parameters, the X-ray line profiles are modeled with our 2-D stochastic code. The modeled lines are then compared with the observed lines.

The paper is organized as follows. Observational evidences of strong wind clumping are discussed in Section 2. The observations and broad-band spectral properties of our sample stars are presented in Section 3. The analysis of line ratios of He-like ions, conducted in order to estimate the location and temperature of the X-ray emitting plasma, is presented in Section 4. Section 5 briefly summarizes our radiative transfer technique for X-rays in a clumped stellar wind. The comparison of modeled and observed line profiles is done in Section 6, and a discussion follows in Section 7.

2 CLUMPED WINDS OF EARLY-TYPE STARS

There is mounting observational evidence of strong inhomogeneity of stellar winds. Stochastic variable structures in the He II 4686 Å emission line in ζ Pup were revealed by Eversberg et al. (1998) and explained as an excess emission from the wind clumps. Markova et al. (2005) investigated the line-profile variability of Hα for a large sample of O-type supergiants. They concluded that the properties of the Hα variability can be explained by a wind model consisting of coherent or broken shells. Bouret et al. (2005) conducted a quantitative analysis of the far-ultraviolet spectrum of two Galactic O stars using the stellar atmosphere code CMFGEN. They have shown that homogeneous wind models could not match the observed profiles of O V and N IV and the phosphorus abundance. However, the clumped wind models match well all these lines and are consistent with the Hα data. This study provides strong evidence of wind clumping in O stars starting just above the sonic point. A reduction of mass-loss rates by a factor of at least 3 compared to the homogeneous wind model is suggested. A similar result was obtained from fitting stellar wind profiles of the P V resonance doublet by Fullerton et al. (2005). A sample of 40 Galactic O-stars was studied, and the conclusion was drawn that the mass-loss rates shall be reduced by up to one order of magnitude, depending on the actual fraction of P V in the wind. The discordance was attributed to the strong clumping of the stellar winds.

X-ray observations of massive stars allow to probe the column density of the wind. An analysis of the X-ray emission from the O stars δ Ori (Miller et al. 2002) and ζ Pup (Kramer et al. 2003) have shown that the attenuation by the stellar wind is significantly smaller than expected from standard homogeneous wind models.

Similar conclusions are reached from the analysis of X-rays from colliding wind binaries (CWB). Such systems consist of two massive early-type stars. The copious X-ray emission is produced in the wind collision zone. At certain orbital phases the X-ray emission from the colliding wind zone travel towards the observer through the bulk of the stellar wind of one companion. Deriving the absorbing column density from X-ray spectroscopy constrains the mass-loss rates. An analysis of XMM-Newton observations of the massive binary γ^2 Vel was presented by Schild et al. (2004). They showed that the observed attenuation of X-rays is much weaker than expected from smooth stellar wind models. To reconcile theory with observation, Schild et al. (2004) suggest that the wind is strongly clumped. Similar conclusions were reached from Chandra and RXTE observations of WR 140 (Pollock et al. 2005). Alike γ^2 Vel, the column density expected from the stellar atmosphere models that account for clumping in first approximation only is a factor of four higher than the column density inferred from the X-ray spectrum analysis.

Table 1. Chandra ACIS-S HETGS observations of prominent O-type stars

Name	ObsID	$\log(N_{\rm H})$ [cm^{-2}]	Flux [erg/s/cm^2]	exposure [ksec]
ζ Pup	640	20.00	8.5×10^{-12}	67
ζ Ori	610	20.48	1.0×10^{-11}	59
ζ Ori	1524	20.48	1.0×10^{-11}	13
ξ Per	2450	21.06	1.6×10^{-12}	160
ζ Oph	4367	20.78	3.1×10^{-12}	48
ζ Oph	2571	20.78	3.1×10^{-12}	35

Table 2. Stellar wind parameters from Repolust et al. (2004) and Lamers et al. (2001)

Name	Sp.Type	R_* [$R_\odot$]	$T_{\rm eff}$ [kK]	v_∞ [km/s]	$\dot{M}$ [$M_\odot\,{\rm yr}^{-1}$]
ζ Pup	O4I	19.4	39	2250	9.0×10^{-6}
ζ Ori	O9.5I	31	32	2100	2.5×10^{-6}
ξ Per	O7.5III	14.0	35	2450	1.8×10^{-6}
ζ Oph	O9V	8.9	32	1550	$\leqslant 1.8 \times 10^{-7}$

Spectacular evidence of wind clumping comes from X-ray spectroscopy of high-mass X-ray binaries (HMXB). In some of these systems a neutron star is on a close orbit deeply inside the stellar wind of an OB star. The X-ray emission with a power-law spectrum results from Bondi-Hoyle accretion of the stellar wind onto the NS. These X-rays photoionize the stellar wind. The resulting X-ray spectrum shows a large variety of emission features, including lines from H-like and He-like ions and a number of fluorescent emission lines. Sako et al. (2003) reviewed spectroscopic results obtained by X-ray observatories for several wind-fed HMXBs. They conclude that the observed spectra can be explained only as originating in a clumped stellar wind where cool dense clumps are embedded in rarefied photoionized gas. Van der Meer et al. (2005) studied the X-ray light curve and spectra of 4U 1700-37. They showed that the feeding of the neutron star by a strongly clumped stellar wind is consistent with the observed stochastic variability.

These observational findings appear to be consistent with the stellar wind theory. The hydrodynamic modeling of Feldmeier et al. (1997) predicts that the stellar winds are strongly inhomogeneous

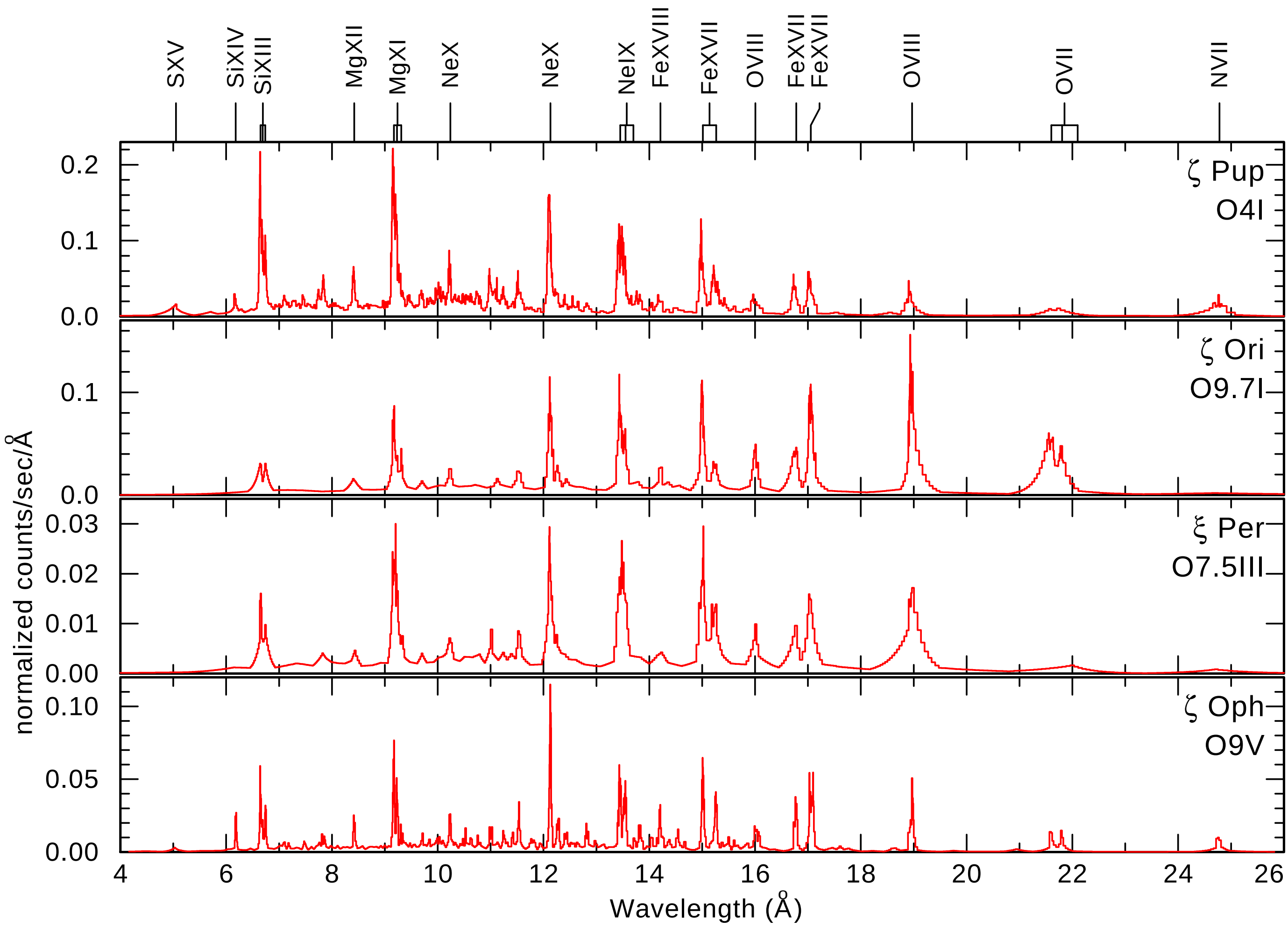

Figure 1. De-reddened HETGS/MEG±1 spectra of prominent O stars. "Normalized" is defined such that when multiplying the vertical axes by the useful exposure time, one obtains the total counts.

starting from close to the core, and with large density, velocity and temperature variations due to the de-shadowing instability. This instability leads to strong gas compression resulting in dense cool shell fragments (clumps). The space between fragments is essentially void, but at the outer side of the dense shells exist extended gas reservoirs. Small gas cloudlets are ablated from these reservoirs, and accelerated to high speed by radiation pressure. Propagating through an almost perfect vacuum, they catch up with the next outer shell and ram into it. In this collision, the gas parcels are heated and emit thermal X-rays. The X-ray emission ceases when the wind reaches its terminal speed. In contrast, the cool fragments are maintained out to large distances. Runacres & Owocki (2005) studied the 1-D evolution of instability-generated structures in the winds and demonstrated that the winds are inhomogeneous out to distances of $1000\,R_*$. Thus theory predicts the existence of two disjunctive structural wind components – hot gas parcels that emit X-rays, and highly compressed cool fragments that attenuate this radiation.

3 HIGH-RESOLUTION X-RAY SPECTROSCOPY OF SINGLE O STARS

A growing number of O-type stars has been observed with the high-resolution spectrographs on board of Chandra and XMM-Newton. The purpose of this paper is to study the X-ray line profiles, therefore we selected the brightest stars with well-resolved lines. The HETGS/HEG detector on board of Chandra has a spectral resolution $\Delta\lambda = 0.012$ Å, while HETGS/MEG has $\Delta\lambda = 0.024$ Å. However the effective area of HEG is smaller than that of MEG. The RGS on XMM-Newton has larger effective area but covers a narrower band at more modest resolution. For consistency we concentrate here only on the first order co-added HETGS/MEG spectra.

We consider only single stars because in a CWB the geometry of the system can affect the line shapes (Henley et al. 2003). However, there is no way to make sure that an O star is definitely single. Runaway O stars are distinguished by an almost complete lack of multiplicity (Hoogerwerf et al. 2001). Therefore, we have selected all three single O-type runaways observed by Chandra HETGS – ζ Pup, ξ Per, and ζ Oph. These stars are relatively X-ray bright and observed with exposures long enough to accumulate high quality spectra as shown in Table 1 and in Fig. 1. We have also considered a fourth star, ζ Ori, albeit it is a known binary (Hummel et al. 2000), because the initial interpretation of X-ray emission line pro-

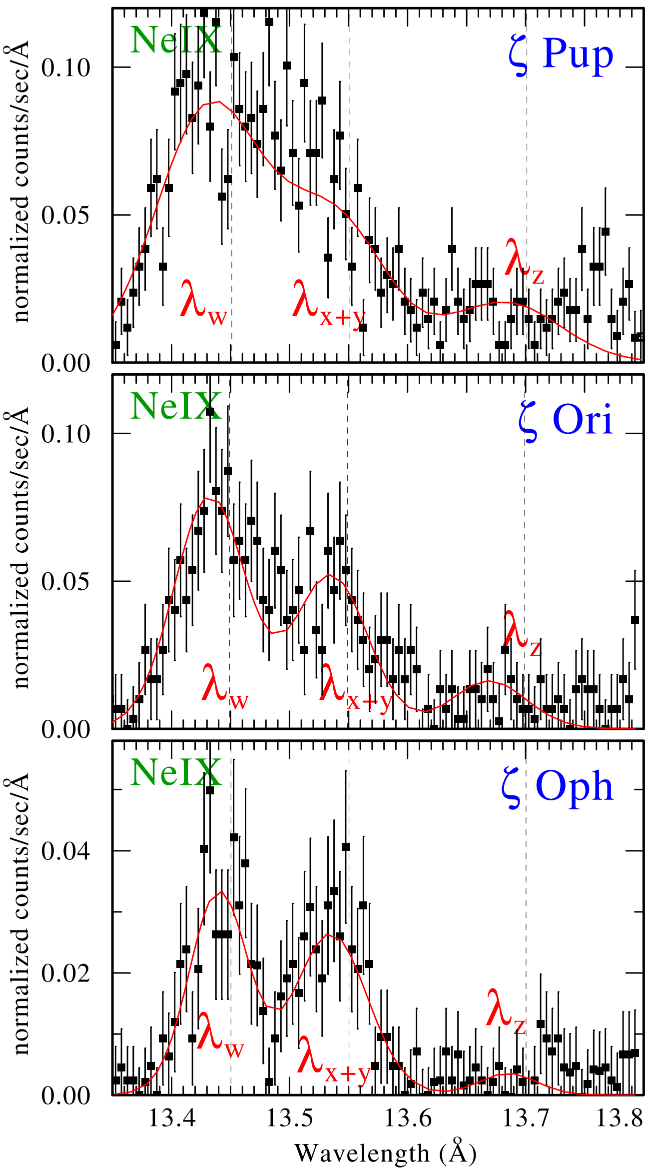

Figure 2. The co-added MEG±1 spectrum of ζ Pup, ζ Ori and ζ Oph at the Ne IX line. Vertical dashed lines indicate rest-frame wavelength: λ_w – resonant line, λ_{x+y} – intercombination line, λ_z – forbidden line. The rest frame wavelengths in this and all following figures are corrected for the radial velocities taken from Hoogerwerf et al. (2001). The solid lines are triple-gaussians fits.

files from this star caused doubts in the validity of the shock model of X-ray production (Waldron & Cassinelli 2001). The stellar and wind parameters of our sample stars are compiled in Table 2.

Waldron & Cassinelli (2001) presented a detailed analysis of Chandra observations of ζ Ori. Cassinelli et al. (2001) and Kramer et al. (2003) analyzed Chandra spectra of ζ Pup. XMM-Newton observations of ζ Pup were analyzed by Kahn et al. (2001). Waldron (2005) reported observations of ζ Oph. Chandra observations of ξ Per were not yet published to our knowledge.

We retrieved the public archival data of these four stars and extracted the spectra using the latest versions of the Chandra software and the calibration data base. The de-reddened MEG spectra of the stars are shown in Fig. 1 (see also XMM-Newton spectra of O stars in Fig. 8 from Paerels & Kahn (2003)). The emission lines seen in all spectra are resolved, with broader lines seen in the stars with higher wind velocities. The spectra exhibit emission from H-like and He-like ions of low and intermediate Z elements. The Si and Mg lines are most prominent in the ζ Pup spectrum, while oxygen lines dominate the spectrum of ζ Ori. The ratio of nitrogen to oxygen line fluxes is higher in the runaway stars compared to the ζ Ori spectrum. Kahn et al. (2001) found that in ζ Pup the emission measures derived from the nitrogen emission lines are at least one order of magnitude larger that those of carbon and oxygen. They conclude that the elemental abundance ratios of nitrogen to oxygen, as well as nitrogen to carbon are considerably higher than solar indicating that the material has undergone CNO processing. This is in accordance with scenarios where runaways have previously been members of close binary systems and undergone mass exchange.

The spectral energy distribution (SED) of all stars can be reproduced using the standard fitting software, e.g *xspec*. The model that accounts for both thermal bremsstrahlung and line emission provides the best fit to the SED of ζ Pup. Kahn et al. (2001) have also reported the detection of continuum in the XMM-Newton spectrum of ζ Pup, although their fits were inconclusive. The temperature estimates from the emission-line and the continuum models are similar, $kT_X \approx 0.6$ keV.

The emission lines seen in the spectra of O stars cannot be fitted by means of the stationary plasma emission line models implemented in the fitting software. The standard models are not adequate for the fast moving stellar winds, and cannot predict expected line profiles.

4 LINE RATIOS FOR HELIUM-LIKE IONS

The He-like ions show characteristic "*fir* triplets" of a forbidden (z), an intercombination ($x+y$) and a resonance (w) line. In OB type stars, the *fir* line ratios can be used to constrain the temperature and location of the X-ray emitting plasma. As was shown by Gabriel & Jordan (1969) the ratios $R(n_e)$ and $G(T_e)$ are sensitive to the electron density and to the electron temperature:

$$R(n_e, T_{rad}) = \frac{z}{x+y} \tag{1}$$

$$G(T_e) = \frac{z+(x+y)}{w} \tag{2}$$

A strong radiation field can lead to a significant depopulation of the upper level of the forbidden line via photo-excitation to the upper levels of the intercombination lines. This is analogous to the effect of electronic collisional excitation, thus mimicking a high density. For the characteristic densities of O star winds the photo-excitation is the dominant mechanism for depopulation. Since the radiation field dilutes with distance from the stellar surface, the ratio between forbidden and intercombination line provides information about the distance of the X-ray emitting plasma from the photosphere. However, this is possible only when the radiative temperature T_{rad} of the radiation field at the wavelength of the depopulating transition is known. Porquet et al. (2001) performed improved calculations of R and G line ratios for plasmas in collisional equilibrium and tabulated them for a wide range of parameters, including T_{rad}.

Lines of O VII, Ne IX, Mg XI, and Si XIII are observed in all our sample stars, however O VII is well resolved only in ζ Oph. Therefore, we use in our analysis only He-like ions of Ne, Mg, and Si. In the sample stars with large wind velocities, ζ Pup and ξ Per,

Table 3. Ratios of fluxes[1] in the components of He-like ions estimated by fitting observed spectral features.

Star	Ne IX		Mg XI		Si XIII	
	R	G	R	G	R	G
ζ Pup	0.35 ± 0.12	1.3 ± 0.3	0.36 ± 0.09	1.05 ± 0.15	0.9 ± 0.2	1.1 ± 0.2
ζ Ori	0.3 ± 0.2	0.9 ± 0.2	0.9 ± 0.4	1.1 ± 0.3	1.9 ± 1.6	1.4 ± 0.8
ξ Per	0.1 ± 0.1	1.4 ± 0.5	0.19 ± 0.15	1.17 ± 0.35	2 ± 13	1 ± 3
ζ Oph	1.1 ± 1.1	1.13 ± 0.35	0.3 ± 0.1	1.0 ± 0.3	0.9 ± 0.8	0.6 ± 0.3

[1] Fluxes are from the triple-gaussian fitting of MEG spectral lines

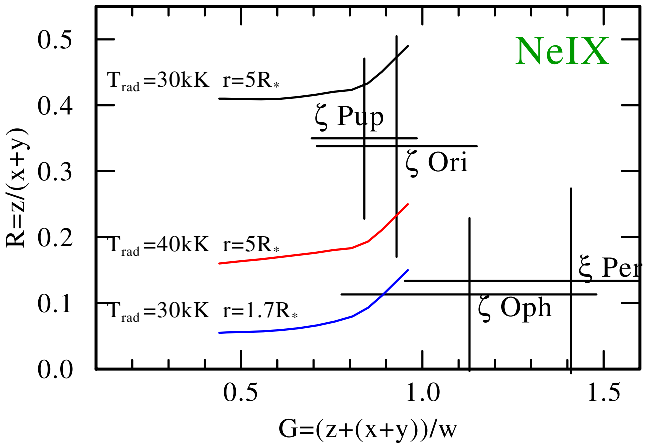

Figure 3. Observed and theoretical R and G ratios for the Ne IX *fir* triplet. Observed values and error bars are taken from Table 3. The curves represent the theoretical R and G from Porquet et al. (2001) for the corresponding $T_{\rm rad}$ and the radii of line formation. Observed values of G are consistent with electron temperatures $T_{\rm e} \lesssim 2$ MK. Observed values of R constrain the line formation region to lie between ≈ 2 and $4\,R_*$ in ζ Pup and ζ Ori, and $\lesssim 2\,R_*$ in ζ Oph and ξ Per.

the $w, x+y$, and z components strongly overlap. Hence flux estimates in each separate component are ambiguous. The situation is best for ζ Oph, the star with the lowest wind velocity, where all components are well separated. To obtain the flux in the w, $x+y$, and z components for a given ion, we have fitted all three components simultaneously as gaussians. Figure 2 shows an example of the observed and fitted lines of a He-like ion. The derived R and G ratios for all stars are listed in Table 3.

The tables from Porquet et al. (2001) were used to constrain the temperature and location of the X-ray emitting plasma. The ratio G is sensitive to $T_{\rm e}$, while it is almost insensitive to $n_{\rm e}$, $T_{\rm rad}$ and the dilution factor W. In our stars G is large. The derived electron temperatures are lower than the temperatures corresponding to the ionization potential for the given ion. The emission measures are highest for the ions with lowest ionisation potential. This is in accordance with the analysis of differential emission measure in ζ Pup and ζ Ori conducted by Wojdowski & Schulz (2005).

In the winds of O stars the electron density does not exceed $\sim 10^{10}\,{\rm cm}^{-3}$, even close to the stellar photosphere. For electron densities less than $\sim 10^{12}\,{\rm cm}^{-3}$ and in the presence of a strong UV field, the ratio R (forbidden to intercombination lines) is not sensitive to the density but depends instead on the electron temperature $T_{\rm e}$, radiative temperature $T_{\rm rad}$, and the dilution factor W.

The electron temperature is constrained by G. The radiative temperature of the radiation field at the wavelength of interest (see Table 3 in Porquet et al. (2001)) can be determined from stellar atmosphere models. Repolust et al. (2004) analyzed Galactic O star sample by means of line-blanketed NLTE model atmospheres. They calculated the radiation temperature as function of wavelength (see their Fig. 11). Based on their models we estimate the radiative temperature at $\lambda_{\rm f\rightarrow i}$ 864 Å (Si XIII) as $\lesssim$ 90 per cent of the effective temperature. For the lighter ions $\lambda_{\rm f\rightarrow i}$ 1033 Å (Mg XI), $\lambda_{\rm f\rightarrow i}$ 1270 Å (Ne IX), the wavelength of interest is on the red side of the Lyman jump in the stellar SED, and the radiative temperature is higher, roughly equal to the effective temperature. The effective temperatures of our stars are listed in Table 2.

With $T_{\rm rad}$ and $T_{\rm e}$ constrained, the ratio R can be used to estimate the dilution factor W and, therefore, the radial distance r from the stellar photosphere at which the X-rays are produced. The ratios R and G and corresponding error bars measured in Ne IX for our sample stars are shown in the $R-G$ diagram in Fig. 3. From Table 2, the effective temperatures for our sample stars are between 30 and 40 kK. The radiative temperatures at λ 1270 Å are a few per cent lower. Theoretical values of R and G, calculated by Porquet et al. (2001) for $T_{\rm rad} = 30$ kK and $T_{\rm rad} = 40$ kK, and for different distances r, are also plotted in Fig. 3. From comparison of observed and theoretical values R and G we may conclude that the NeIX line is emitted by gas located between $2\,R_*$ and $5\,R_*$ in ζ Pup and ζ Ori, and close to $2\,R_*$ in ζ Oph and ξ Per. Similar diagrams were also constructed for Mg XI and Si XIII. Data for Mg XI indicate the presence of X-ray emission at $\lesssim 2\,R_*$ for all stars except ζ Ori, where the radius of emission is somewhat larger, $r \lesssim 3-4\,R_*$. Si XIII lines were sufficiently well resolved only in ζ Pup and ζ Oph. As can be inferred from the $R-G$ diagram for Si XIII, the line formation region is located at $r \lesssim 2\,R_*$.

Overall, the analysis of line ratios in He-like ions indicates that the line formation regions are located relatively close to the stellar surface for all stars of our sample.

5 TRANSFER OF X-RAYS IN A CLUMPED STELLAR WIND

Wind inhomogeneity alters the radiative transfer significantly. We have studied the effects of wind fragmentation on X-ray line formation analytically in the limit of infinitely many stochastically distributed fragments (Feldmeier et al. 2003), and numerically for a finite number of fragments within an accelerating stellar wind (Oskinova et al. 2004). The latter work describes in detail the model and the code used in the present paper. Here we briefly summarize the description of fragmented-wind opacity in order to introduce

© 2006 RAS, MNRAS **000**, 1–11

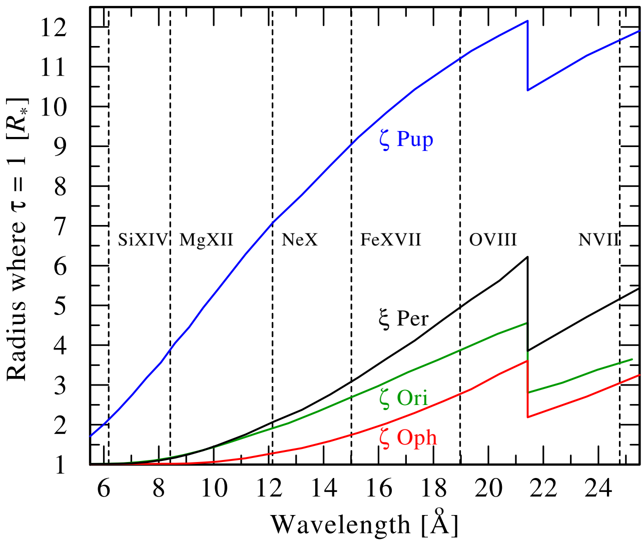

Figure 4. The radius were the radial optical depth of the wind becomes unity in dependence on the wavelength in the Chandra HETGS/MEG range. The calculations were done using the PoWR stellar atmosphere code (see text) with stellar parameters from Table 2. The prominent edge at λ 21.5 Å is due to oxygen. The vertical dashed lines correspond to the rest wavelength of the indicated ions.

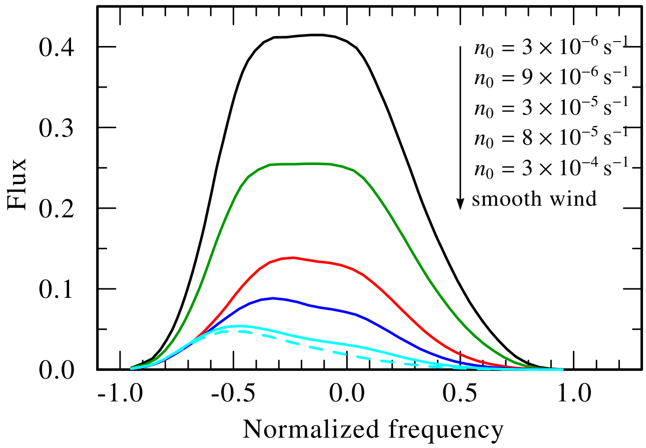

Figure 5. Solid lines: model line profiles of O VIII in the spectrum of ζ Ori for different number of clumps in the wind. The fragmentation frequency, n_0, is indicated. Corresponding average number of fragments in radial direction is $\langle N_\mathrm{r}\rangle = 10, 30, 100, 300, 1000$ from the top to the bottom. Dashed line: model line from the smooth wind model. The line formation region is assumed between $1.7R_*$ and $5R_*$, velocity law is with $\beta = 1$. Frequency is measured relative to the line center and in Doppler units referring to the terminal wind velocity v_∞.

the parameters that will be used in the next section to model observed X-ray lines.

We introduce Cartesian coordinates where the z axis points towards the observer and the impact parameter p stands perpendicular to the latter. Alternatively, a point (p, z) is specified by spherical coordinates, i.e. the radius $r = \sqrt{p^2 + z^2}$ and the angle $\vartheta = \cos^{-1}\mu$ between the line of sight and the radial vector. Hence $\mu = z/r$. It is assumed that the time-averaged stellar wind is spherically symmetric and expands with a radius-dependent velocity

$$v(r) = v_\infty \left(1 - \frac{r_0}{r}\right)^\beta , \tag{3}$$

where v_∞ is the terminal velocity, and r_0 is chosen such that $v(r = R_*) = 0.01\,v_\infty$. R_* is the stellar (photospheric) radius. For a given mass loss rate $\dot{M}$, the continuity equation defines the density stratification via $\rho(r) = \dot{M}/(4\pi r^2 v(r))$.

We consider *continuum* absorption of X-rays caused predominantly by bound-free and K-shell ionisation processes. The wind can be specified by its total radial optical depth,

$$\tau_* = \int_{R_*}^{\infty} \kappa_\nu \rho(r)\,\mathrm{d}r , \tag{4}$$

where κ_ν is the mass absorption coefficient which can be calculated from the chemical composition, population numbers and the continuum cross sections at the energy of the considered X-ray line. For a homogeneous wind, the optical depth $\tau_\mathrm{h}(p, z)$ between a point (p, z) and the observer is

$$\tau_\mathrm{h}(p, z) = \frac{\kappa_\nu \dot{M}}{4\pi} \int_z^\infty \frac{\mathrm{d}z'}{r'^2 v(r')} . \tag{5}$$

with $r' = \sqrt{p^2 + z'^2}$.

We assume that close to the stellar core at distances smaller than $r_\mathrm{sh}^\mathrm{min} \lesssim 2R_*$ the wind is homogeneous and no X-ray production is taking place. The wind instabilities start to develop at the distances larger than $r_\mathrm{sh}^\mathrm{min}$. These instabilities result in the heating of some small fraction of the material to X-ray emitting temperatures. The general stellar wind remains cool and is compressed into shell fragments. While general wind fragmentation persists till large distances $r_\mathrm{sh}^\mathrm{max} \approx 300R_*$, the X-ray emission is ceased at the distance $r_\mathrm{em} \gtrsim 10R_*$.

The hot material ($T_\mathrm{X} \sim 1\,\mathrm{MK}$) emitting X-rays is permeated with the cool ($T_\mathrm{w} \sim 10\,\mathrm{kK}$) wind fragments (i.e. clumps), which attenuate the X-ray emission. Both the hot and the cool gas component move outwards with the same velocity $v(r)$. The mass and the solid angle of each fragment are preserved. The cool fragments are compressed radially and therefore aligned (this model sometimes is referred to as "Venetian blinds" model).

In order that the time-averaged mass-flux $\dot{M}$ of shells resembles that of a stationary, homogeneous wind, the radial number density of shells must scale with $1/v(r)$:

$$n(r) = \frac{n_0}{v(r)} . \tag{6}$$

The parameter $n_0 = n(r)v(r)$ can be considered as the number of fragments passing through some reference radius (e.g. entering or leaving the wind) per unit of time. It does not depend on the distance and is therefore convenient model parameter. We refer to n_0 as *fragmentation frequency*.

When n_0 is specified, the time averaged number of fragments in radial direction is

$$\langle N_\mathrm{r}\rangle = n_0 \int \frac{\mathrm{d}r}{v(r)}. \tag{7}$$

As was discussed in Oskinova et al. (2004), the average *radial* optical depth of a fragment located at distance r is

$$\bar{\tau}_j^\mathrm{rad} = \frac{\kappa_\nu \dot{M}}{4\pi} \cdot \frac{1}{r^2} \cdot \frac{1}{n_0}, \tag{8}$$

and the optical depth along the line-of-sight p =const is

$$\bar{\tau}_j = \frac{\bar{\tau}_j^\mathrm{rad}}{|\mu|}, \tag{9}$$

where

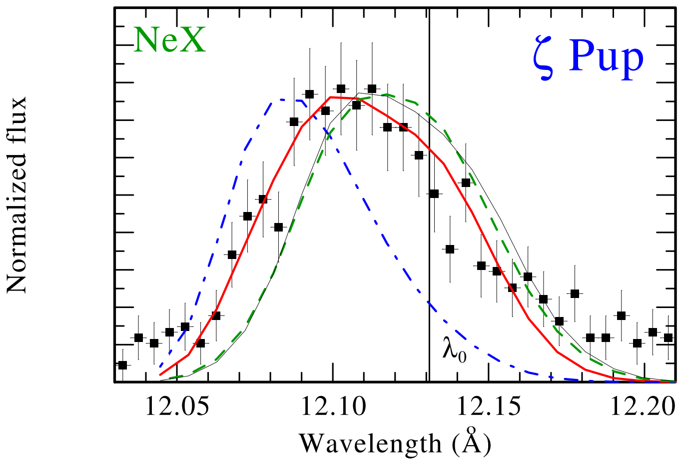

Figure 6. Observed (co-added MEG±1) and modeled Ne X line in ζ Pup. The model lines are calculated assuming the emission origins between $2R_*$ and $5R_*$ and the velocity law has $\beta = 1.1$. The thick solid line represents a model with $n_0 = 1.6 \times 10^{-4}\ \mathrm{s}^{-1}$ ($\langle N_r \rangle = 300$). The dashed line is for the model with $n_0 = 2.6 \times 10^{-5}\ \mathrm{s}^{-1}$ corresponding to $\langle N_r \rangle = 50$ shells in radial direction on average. The dash-dotted line is for the smooth wind model. All lines except the thin smooth line are calculated using $\dot{M} = 9 \times 10^{-6}\ M_\odot\ \mathrm{yr}^{-1}$. For the thin smooth line $\dot{M} = 4.4 \times 10^{-7}\ M_\odot\ \mathrm{yr}^{-1}$ is assumed as in Fullerton et al. (2005).

$$|\mu| = \frac{z_j}{\sqrt{p^2 + z_j^2}}. \tag{10}$$

The optical depth along the line of sight between point (p, z) and the observer in a stellar wind which consists of aligned fragments is

$$\tau(p, z) = n_0 \int_z^\infty (1 - \mathrm{e}^{-\bar{\tau}_j})\, |\mu(r')|\, \frac{\mathrm{d}z'}{v(r')}, \tag{11}$$

where $\mathrm{d}z' = \mathrm{d}r'/\mu$.

We can compare the optical depth in a fragmented wind (Eq. 11) with the optical depth in a homogeneous wind (Eq. 5). In the limiting case of optically thin fragments ($\bar{\tau}_j^{\mathrm{rad}} \ll 1$) the exponent under the integral in Eq. (11) can be expanded. Substituting the average optical depth of a fragment defined by Eq. (9), one can see that the optical depth in the thin-fragment limit is the same as in a homogeneous wind.

In the limit of optically thick fragments ($\bar{\tau}_j^{\mathrm{rad}} \gg 1$) the optical depth becomes

$$\tau(p, z) = n_0 \int_r^\infty \frac{\mathrm{d}r'}{v(r')}, \qquad \tau_j \gg 1\,. \tag{12}$$

Here the dependence on the mass absorption coefficient κ_ν and $\dot{M}$ has disappeared. In a wind with optically thick fragments the opacity is grey and is determined only by the fragmentation frequency n_0 and the wind velocity.

In our stochastic wind model the fragments may have different optical depths. As can be seen from Eq. (11) the dependence of optical depth $\tau(p, z)$ on κ_ν is weak compared to the homogeneous case (Eq. 5). Hence, albeit the opacities κ_ν differ significantly depending on the wavelength (see Table 4), the optical depths $\tau(p, z)$ for different lines remains similar (more so in the case of optically thick clumps). Therefore the profiles of different X-ray lines do not change across the spectrum.

Table 4. Mass absorption coefficient κ_ν [g cm^{-2}] at the wavelengths of X-ray emission lines from stellar wind models, for the radial range between $2R_*$ and $5R_*$

Line	Wavelength [Å]	ζ Pup	ζ Ori	ξ Per	ζ Oph
Si XIV	6.18	18	34	11	11
Mg XII	8.42	22	44	23	23
Ne X	12.14	59	73	55	57
Fe XVII	15.01	94	108	95	95
O VIII	18.97	171	177	170	172
N VII	24.78	93	80	93	94

6 COMPARISON WITH OBSERVED X-RAY LINE PROFILES

6.1 Parameters of the model

We used the stellar parameters listed in Table 2 and the relevant abundances to calculate the wind opacity. This is done by means of PoWR stellar atmosphere models (Hamann & Gräfener 2004). Values of κ_ν derived for each star in our sample at the wavelengths of strongest emission lines are shown in Table 4. The stellar parameters determined from the atmosphere models for each star, $\dot{M}$, v_∞, κ_ν, and R_*, are fixed in our modeling.

The PoWR atmosphere model does account for clumping in a first approximation, i.e. assumes numerous optically thin clumps. In our clumped wind model the mass-loss rate in each radial direction is identical and the radial optical depth is the same as calculated by PoWR model of the same mass-loss rate. To get an idea how transparent the stellar wind is for X-ray radiation, it is illustrative to consider at which radius the radial optical depth becomes unity. Using PoWR models we calculate these radii in dependence on wavelength and show them in Fig. 4. From the *fir* analysis the upper limit on the location of X-ray production region was estimated at $\approx 5R_*$ (see Section 4). As can be seen from Fig. 4 the wind is optically thick for all lines in ζ Pup (except perhaps Si XIV). The wind is also optically thick at some wavelengths in ξ Per and ζ Ori, while it is optically thin for all lines in ζ Oph.

For a spherically symmetric, radial flow, the width of a line provides information about the velocity of the emitting material. With known velocity field this may be translated to radii. For the velocity field parameter β we choose a value between 0.9 and 1.5 for each star. Given the quality of the data and the number of free parameters in the model, the velocity law is somewhat uncertain and affects the estimate of the radial zone where X-rays are produced.

The key parameter of the model is the fragmentation frequency n_0, which describes the degree of clumping. The dependence of the line shape on n_0 is demonstrated in Fig. 5, where the model line profiles for the O VIII line in the spectrum of ζ Ori are shown. All profiles are calculated with $\beta = 1.0$, line formation region between $1.7R_*$ and $6R_*$, and the same τ_*, but with different fragmentation frequencies n_0 as indicated. One can see from Eq. (8) that when n_0 is small the fragments are optically thick and effectively opaque for X-rays. In this case the radiation can escape only between fragments and the shape of the line profile does not change as long as the fragments remain opaque. However, when n_0 grows, more fragments become optically thin and the line shape

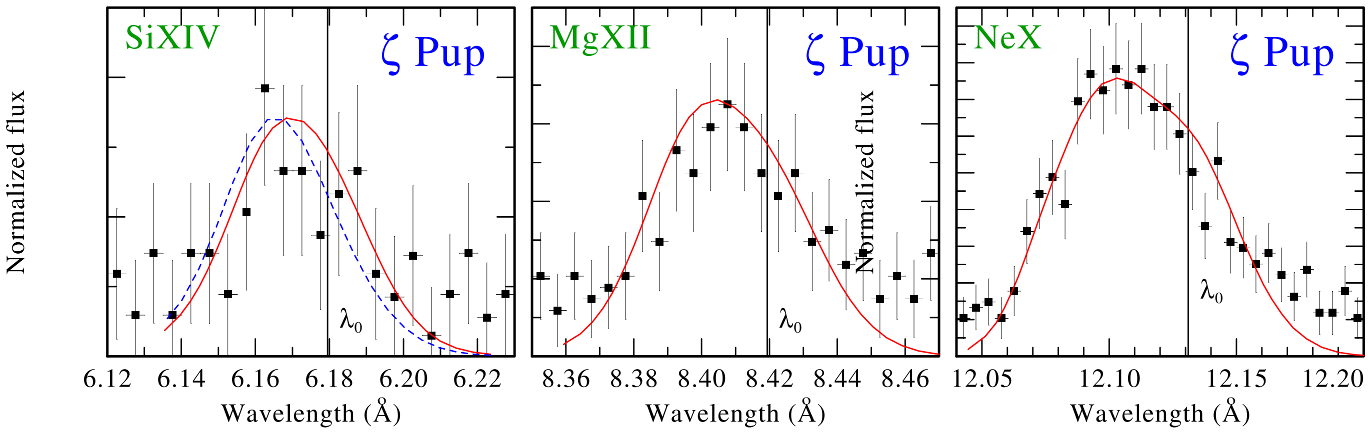

Figure 7. Lines observed in ζ Pup (co-added MEG±1) and the model lines. The solid lines are the model with $n_0 = 1.6\times10^{-4}\,\mathrm{s}^{-1}$ ($\langle N_r\rangle = 300$), $\beta = 1.1$, and the radiation originating between $2R_*$ and $5R_*$. The adequate cool-wind opacity κ_ν from PoWR NLTE model was used for each line. Dashed line is for the homogeneous model of the same $\dot{M}$.

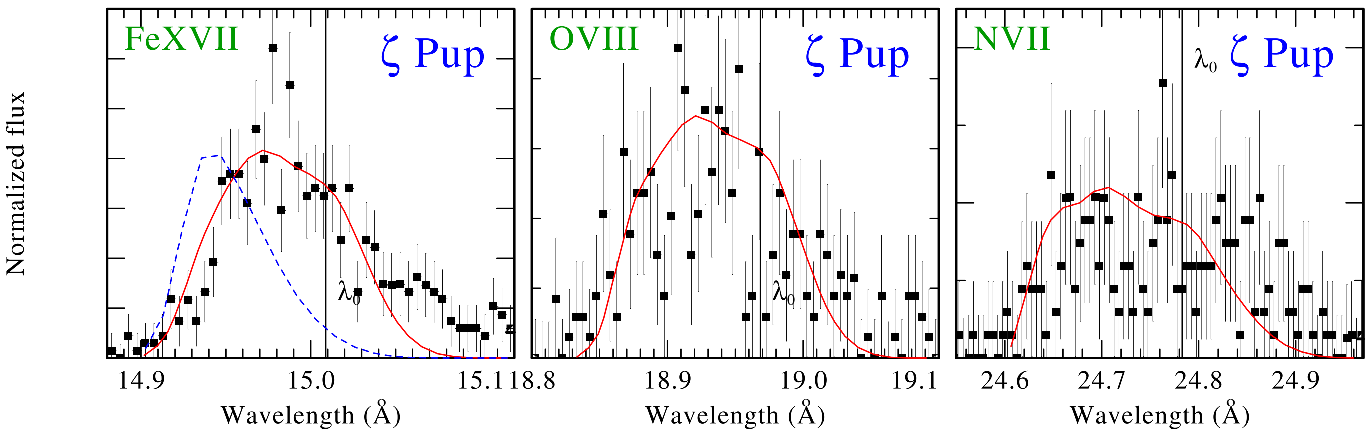

Figure 8. The same as in the Fig. 7 except NVII line. In order to roughly reproduce the line shape we assumed that the radiation in this line originates between $2R_*$ and $12R_*$.

changes. For sufficiently large n_0, the line approaches the shape predicted by the smooth wind model.

6.2 X-ray emission lines in ζ Pup, ξ Per, ζ Ori, and ζ Oph

ζ **Pup.** The model lines shown in Fig. 6 are scaled in height to the Ne X line observed in ζ Pup. The shape of the observed line can be reproduced assuming $n_0 = 2.6\times10^{-5}\,\mathrm{s}^{-1}$ ($\langle N_\mathrm{r}\rangle = 300$). As can be seen in Fig. 6 the lines resulting from a model with fewer but more opaque fragments ($\langle N_\mathrm{r}\rangle = 50$) and from a smooth wind model do not match the observed line. Recently, Fullerton et al. (2005) revised the ζ Pup mass-loss rate down to $4.4\times10^{-7}\,\dot{M}\,\mathrm{yr}^{-1}$ based on their analysis of the P V line. The model line calculated with this $\dot{M}$ is also shown in Fig. 6. The model has too small blueshift compared with the observed line, indicating too low continuum attenuation. On this basis we suggest that the mass-loss rate in ζ Pup is higher than estimated by Fullerton et al. (2005).

Figure 7 shows the strongest emission lines observed in ζ Pup together with the model lines.Parameters of ζ Pup are from Table 2, $\beta = 1.1$ is assumed. The line formation region is assumed to lie between $2R_*$ and $5R_*$. The lines are broadened up to $\pm\,0.8\,v_\infty$. As can be seen in Fig. 4, the wind of ζ Pup is optically thin for the X-rays at the Si XIV $\lambda 6.18$Å line just above $2R_*$. When the wind is optically thin above the line formation region, the emergent line shall be nearly symmetric relative to the rest wavelength λ_0. However, the peak of the Si XIV line is shifted to the blue, quite similar to other lines in Fig. 7. This indicates that the line photons must have originated below the surface of optical depth unity at $2R_*$. This is in agreement with the estimates based on the *fir* analysis.

The clumped wind model predicts that the shape of the emission lines is similar across the spectrum. This prediction is confirmed observationally. Kramer et al. (2003) note from the analysis of observed lines, that the amount of absorption inferred for different lines in ζ Pup, and the line shapes are not sensitive to wavelength. An exception is the N VII line, which is the only line with box-like shape. The line is broadened up to the $\pm\,v_\infty$. Kahn et al. (2001) observe that the line shows evidence for resolved, discrete structure.

ξ **Per.** The strongest X-ray emission lines observed in ξ Per are shown in Fig. 9. The data are quite noisy and it is difficult to constrain the model parameters. However, the lines in ξ Per look similar to each other regarding broadening and blueshifts. For comparison, we have over-plotted on the Fe XVII line both smooth and fragmented model line profiles. The lines are broadened up to $\pm\,0.9\,v_\infty$. Assuming $\beta = 0.9$ and the line formation region to lie between $1.7R_*$ and $7R_*$, the model with $n_0 = 7.8\times10^{-5}\,\mathrm{s}^{-1}$

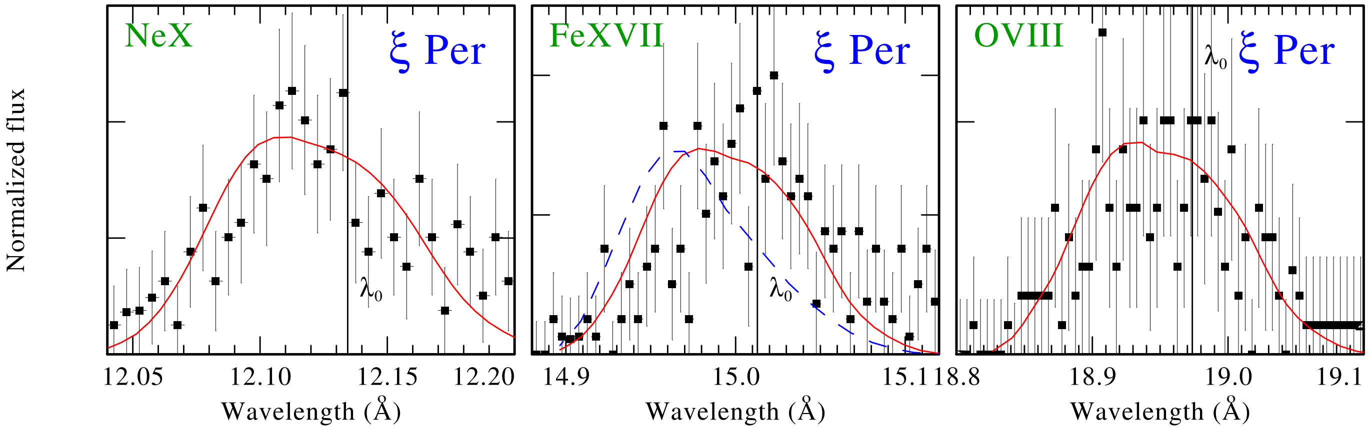

Figure 9. Lines observed in ξ Per (co-added MEG±1) and the model lines. The solid lines are the model with $n_0 = 7.8\times10^{-5}\,\mathrm{s}^{-1}$ ($\langle N_r\rangle = 100$), $\beta = 0.9$, and the radiation originating between $1.7R_*$ and $7R_*$. The adequate cool-wind opacity κ_ν from PoWR NLTE model was used for each line. Dashed line is for the homogeneous model of the same $\dot{M}$.

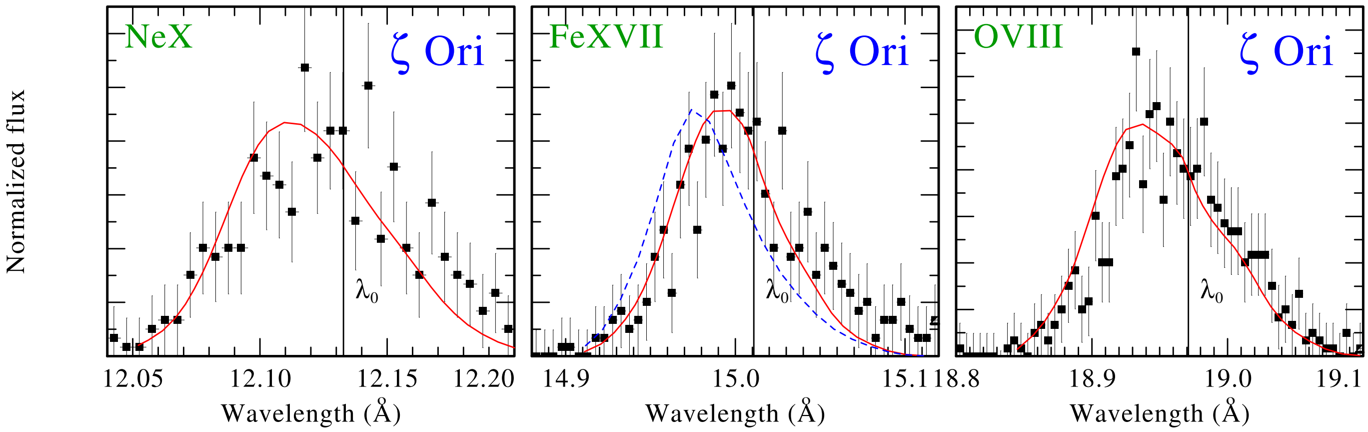

Figure 10. Lines observed in ζ Ori (co-added MEG±1) and the model lines. The solid lines are the model with $n_0 = 2.7\times10^{-5}\,\mathrm{s}^{-1}$ ($\langle N_r\rangle = 100$), $\beta = 0.8$, and the radiation originating between $1.7R_*$ and $9R_*$. The adequate cool-wind opacity κ_ν from PoWR models was used for each line. The dashed line is for the homogeneous model of the same $\dot{M}$.

($\langle N_\mathrm{r}\rangle = 100$) can reproduce the observed lines. Hence, the fragmentation frequency required to fit ξ Per emission lines is slightly smaller than in ζ Pup.

ζ Ori. The same holds for ζ Ori, the star with a thinner wind compared to ζ Pup and ξ Per. Figure 10 shows the best resolved lines in the ζ Ori spectrum. The lines have similar shapes, they are blueshifted and broadened up to the $\pm0.9\,v_\infty$. All lines can be reproduced with $n_0 = 7.8\times10^{-5}\,\mathrm{s}^{-1}$ ($\langle N_\mathrm{r}\rangle = 100$). The line formation region is assumed to lie between $1.7R_*$ and $9R_*$ and we adopt $\beta = 0.8$. Again, for comparison we have over-plotted the smooth wind model profile on the Fe XVII line. Since the wind of ζ Ori is relatively thin, the difference between smooth and fragmented models is not as dramatic as in ζ Pup and ξ Per.

ζ Oph. The wind of ζ Oph is transparent for X-rays. As can be seen in Fig. 4, at the wavelength of the Si XIV, Mg XII, Ne X and Fe XVII the wind is optically thin for the X-rays already above $1.5R_*$. The strongest lines observed in ζ Oph are shown in Fig. 11. Due to the nearly complete lack of absorption in the wind the lines provide information about the location and conditions of the hot plasma itself. The lines are symmetric and quite narrow, with broadening up to the $\pm0.8\,v_\infty$. The slight asymmetry is due to occultation by the stellar core. The line shapes indicate that emission originates in the wind acceleration zone. We adopt $\beta = 1.5$ to reproduce the shape of the emission lines. For the model lines shown in Fig. 11 the line formation region is between $1.5R_*$ and $7R_*$. The origin of X-rays close to the stellar core at $1.5R_*$ is consistent with the results of the *fir* analysis. As can be seen from the two model lines over-plotted on the Fe XVII observed line, the difference between smooth and fragmented models is negligible for the thin wind of ζ Oph.

At the wavelength of the O VIII and the N VII line the wind of ζ Oph is thin above $2.5R_*$. The observed lines are shown in Fig. 12. The O VIII line is asymmetric, with the blue wing being weaker than the red one. The N VII line can be modeled as originating below $2R_*$. To demonstrate how sensitive is the emission line profile to the location of the X-ray emitting plasma, we show two different model line profiles for O VIII and N VII in Fig. 12. It appears that the radiation in the O VIII and the N VII lines is formed slightly further in the wind, at $\approx 1.9\,R_*$.

The ζ Oph wind opacity is small and X-rays produced in the wind can escape without suffering significant attenuation. This allows to assess the intrinsic production of X-rays. We have calculated the ratios of the X-ray luminosity to the bolometric and mechanical($\dot{M}v_\infty^2/2$) luminosity of stellar wind in ζ Oph and compared it with these ratios for other stars. The results are given in

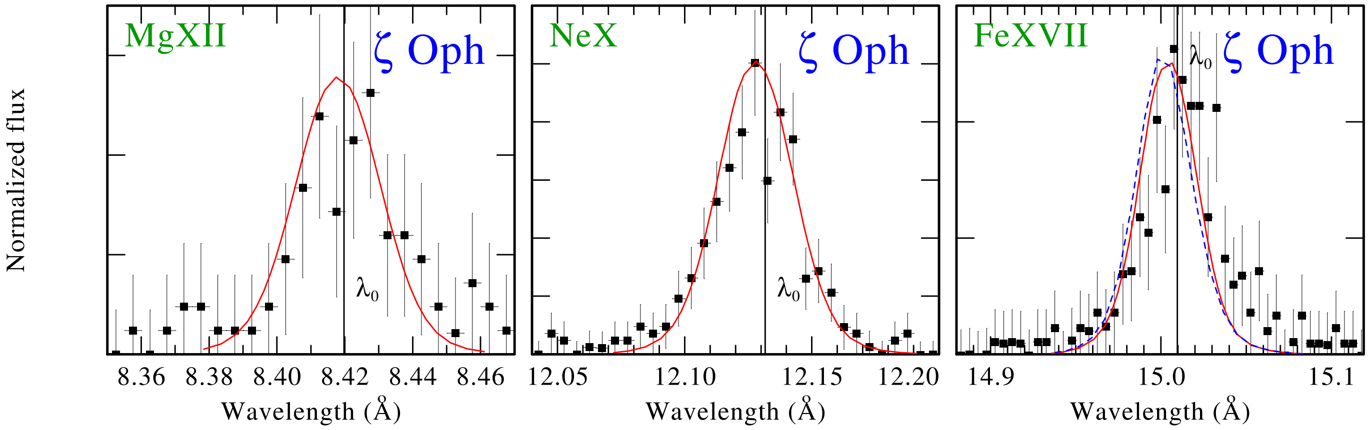

Figure 11. Lines observed in ζ Oph (co-added MEG$\pm$1) and the model lines. The solid lines are the model with $n_0 = 7.7 \times 10^{-5}\,\mathrm{s}^{-1}$ ($\langle N_r \rangle = 100$), $\beta = 1.5$, and the radiation originating between $1.5R_*$ and $7R_*$. The adequate cool-wind opacity κ_ν from PoWR model was used for each line, however in this star the optical depth is smaller than unity for all these lines. Consequently, all lines can be equally well be reproduced by a smooth-wind model (shown by a dashed line).

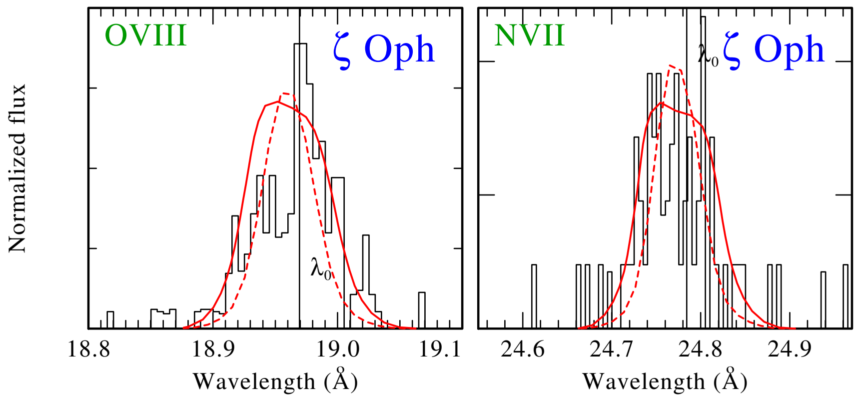

Figure 12. Histograms show the lines of OVIII and NVII observed in ζ Oph (co-added MEG$\pm$1). The model lines are calculated with $\beta = 1.5$ and $n_0 = 7.7 \times 10^{-5}\,\mathrm{s}^{-1}$ ($\langle N_r \rangle = 100$). The solid line is for radiation originating between $1.9R_*$ and $7R_*$, while dashed lines are for the $1.5\,R_* - 7\,R_*$.

Table 5. The ratio of X-ray to bolometric luminosity in all stars is slightly smaller than the canonical 10^{-7} known for OB stars (Berghöfer et al. 1996). Perhaps, this is because the large sample of bright OB stars analyzed by Berghöfer et al. (1996) is biased towards binary stars, which tend to be more X-ray bright.

The ratio of bolometric and mechanical luminosity shown in Table 5 is the same for ζ Pup, ζ Ori, and ξ Per. The X-ray luminosity of ζ Ori was calculated using the same distance as in Lamers et al. (2001). However, if we adopt Hipparcos distance $d = 250$ pc to ζ Ori then $L_X/L_{\mathrm{mech}} = 3.5 \times 10^{-6}$. As can be seen from Table 5 the ratio of the X-ray and the mechanical luminosity is a few times higher in ζ Oph compared to the others stars where attenuation is larger. We estimate that about 0.01% of the kinetic energy of the stellar wind of ζ Oph is spent on the X-ray generation.

7 DISCUSSION

We have applied a model of a clumped stellar wind to reproduce the X-ray emission lines observed in four prominent O stars. By adjusting a small number of free parameters we successfully modeled the observed line profiles.

The effect of clumping on the wind attenuation is threefold. Firstly, it reduces the wind absorption compared to the smooth-wind model, allowing for more flux to escape. Secondly, it leads to a weaker dependence of the effective opacity on wavelength, making it entirely grey in the case of optically thick clumps. This prediction of similar opacity for different lines agrees well with the similarity of line profiles observed at different wavelengths. Thirdly, it affects the shape of line profiles. The radially compressed, slab-like shell fragments lead to the emergence of the symmetric, but blueshifted lines profiles which are indeed observed.

To qualitatively test the more general clump geometry we have also calculated models with spherical clumps. Such model produce emission line profiles which are skewed much as from homogeneous wind models and are in disagreement with the observation.

Inhomogeneity of the stellar wind can reduce the mass-loss rates empirically estimated from the analysis of recombination and Hα lines, but it is presently unknown by which factor. The values discussed in the literature are ranging from factor of two to one order of magnitude. We have conducted test calculation with reduced mass-loss rates for our sample stars. Because the key parameter describing the wind opacity is the fragmentation frequency, the models with $\dot{M}$ reduced by a factor of 2–3 do not differ much from those presented here. However, a model which assumes a 10 times lower mass-loss rate for ζ Pup is too optically thin and does not reproduce the observed line.

By means of PoWR model atmospheres we calculated the

Table 5. Ratios of X-ray, bolometric and mechanical luminosities

Name	D [pc]	L_{X} [erg/s]	L_{bol} [erg/s]	L_{mech} [erg/s]	$L_{\mathrm{X}}/L_{\mathrm{bol}}$	$L_{\mathrm{X}}/L_{\mathrm{mech}}$
ζ Pup	437	2.0×10^{32}	3.0×10^{39}	1.4×10^{37}	6.9×10^{-8}	1.4×10^{-5}
ζ Ori	500	3.6×10^{31}	3.0×10^{39}	2.5×10^{36}	1.2×10^{-8}	1.4×10^{-5}
ξ Per	398	4.9×10^{31}	1.0×10^{39}	3.4×10^{36}	4.9×10^{-8}	1.4×10^{-5}
ζ Oph	154	1.2×10^{31}	2.8×10^{38}	$\leqslant 1.4 \times 10^{35}$	4.1×10^{-8}	$\geqslant 8.5 \times 10^{-5}$

Distances are from Mason et al. (1998)

wind opacity for each of our program stars. It turns out that the wind of ζ Oph is essentially transparent, allowing us to see all intrinsically produced X-rays. We estimate that 0.01% of the mechanical energy of the wind is converted into X-ray emission.

The width of the line profiles allows to estimate at which velocity, and hence in which radius interval, X-rays are produced. This zone of X-ray production can independently be estimated from the analysis of line ratios for helium-like ions. Both methods give consistent results. We find that the X-ray emitting regions are located at moderate radii above the stellar photosphere, where the gas moves with velocities between $0.2\,v_\infty$ and $0.9\,v_\infty$.

Summarizing, we conclude that the model of an inhomogeneous stellar wind, consisting of radially compressed shell fragments, can reproduce the observed X-ray emission lines in O stars. The wind clumping explains the shape of the line *profiles*, i.e. width, symmetry, blueshift as well as the line profiles similarity across the spectrum.

REFERENCES

Berghöfer T.W., Schmitt J.H.M.M., Cassinelli J.P., 1996, A&AS, 118, 481
Bouret J.-C., Lanz T., Hillier D.J., 2005, A&A, 438, 301
Cassinelli J.P., Miller N.A., Waldron W.L., MacFarlane J.J., Cohen D.H., 2001, ApJ, 554, L55
Castor J.I., Abbott D.C., Klein R.I., 1975, ApJ, 195, 157
Eversberg T., Lèpine S., Moffat A.F.J., 1998, ApJ, 494,799
Feldmeier A., Puls J., Pauldrach A.W.A., 1997, A&A, 322, 878
Feldmeier A., Oskinova L., Hamann W.-R., 2003, A&A, 403, 217
Fullerton A.W., Massa D.L., Prinja R.K., 2006, ApJ, in press, astro-ph/0510252
Gabriel A.H., & Jordan C., 1969, MNRAS, 145, 241
Ignace R., 2001, ApJ, 549, L119
Hamann W.-R. & Koesterke L., 1998, A&A, 335, 1003
Hamann W.-R. & Gräfener G., 2004, A&A, 427, 697
Harnden F.R., Jr., et al., 1979, ApJ, 234, L51
Henley D.B., Stevens I.R., Pittard J.M., 2003, MNRAS, 346, 773
Hillier D.J., Kudritzki R.P., Pauldrach A.W., Baade D., Cassinelli J.P., Puls J., Schmitt J.H.M.M., 1993, A&A 276, 117
Hoogerwerf R., de Bruijne J.H.J., Zeeuw P.T., 2001, A&A, 365, 49
Hummel C.A., White N.M., Elias II N.M., Hajian A.R., Nordgren T.E., 2000, ApJ, 540, L91
Kahn S.M., Leutenegger M.A., Cotam J., Rauw G., Vreux J.-M., den Boggende A.J.F., Mewe R., Güdel M., 2001, A&A, 276, 117
Kramer R.H., Cohen D.H., Owocki S.P., 2003, ApJ, 592, 532
Lamers H.J.G.L.M., Haser S., de Koter A., Leitherer C., 1999, ApJ, 516, 872
Lucy L.B. & Solomon P.M., 1970, ApJ, 159, 879
MacFarlane J.J., Cassinelli J.P., Welsh B.Y., Vedder P.W., Vallerga J.V., Waldron W.L., 1991, ApJ, 380, 564
Markova N., Puls J., Scuderi S., Markov H., 2005, A&A, 440, 1133
Mason B.D., Gies D.R., Hartkopf W.I., Bagnuolo W.G.Jr., Brummelaar T.T., McAlister H.A., 1998, AJ, 115, 821
Miller N.A., Cassinelli J.P., Waldron W.L., MacFarlane J.J., Cohen D.H., 2002, ApJ, 577, 951
Oskinova L.M., Feldmeier A., Hamann W.-R., 2004 A&A 422, 675
Owocki S.P. & Rybicki G.B., 1984, ApJ, 284, 337
Paerels F.B.S. & Kahn S.M., 2003, ARA&A
Pollock A.M.T., Corcoran M.F., Stevens I.R., Williams P.M., 2005, ApJ, 629, 482
Pomraning G.C., 1991, Linear kinetic theory and particle transport in stochastic mixtures, Singapore; New Jersey: World Scientific. Series on advances in mathematics for applied sciences 7
Porquet D., Mewe R., Dubau J., Raassen A.J.J., Kaastra J.S., 2001, A&A, 376, 1113
Repolust T., Puls J., Herrero A., 2004, A&A, 415, 349
Runacres M.C. & Owocki S.P., 2005, A&A, 429, 323
Sako M., Kahn S.M., Paerels F., Liedahl D.A., Watanabe S., Nagase F., Takahashi T., 2003, in High Resolution X-ray Spectroscopy with *XMM-Newton* and *Chandra*, ed. G. Branduari-Raymont (astro-ph/p309503)
Schild H., et al., 2004, A&A, 422, 177
Seward F.D., Forman W.R., Giacconi R., Griffiths R.E., Harnden F.R., Jr., Jones C., Pye J.P., 1979, ApJ, 234, L55
van der Meer A., Kaper L., Di Salvo T., et al., 2005, A&A, 432, 999
Waldron W.L. & Cassinelli J.P., 2001, ApJ, 548, L45
Waldron W.L. 2005, To appear in ASP Conf. Ser..”The Nature and Evolution of Disks Around Hot Stars”, 2005
Wojdowski P.S. & Schulz, N.S., 2005, ApJ, 627, 953